The Higgs boson with the ATLAS experiment at the LHC: Discovery, measurement, and searches for new physics

A DISSERTATION PRESENTED
BY
TOMO LAZOVICH
TO
THE DEPARTMENT OF PHYSICS

IN PARTIAL FULFILLMENT OF THE REQUIREMENTS
FOR THE DEGREE OF
DOCTOR OF PHILOSOPHY
IN THE SUBJECT OF
PHYSICS

HARVARD UNIVERSITY
CAMBRIDGE, MASSACHUSETTS
MAY 2016

Thesis advisor: Professor Joao Guimaraes da Costa and Melissa Franklin Tomo Lazovich

The Higgs boson with the ATLAS experiment at the LHC: Discovery, measurement, and searches for new physics

Abstract

We measured things. And searched for other things. Here is what we found, please let me graduate.

Contents

Listing of figures

Listing of tables

This is the dedication.

Acknowledgments

Lorem ipsum dolor sit amet, consectetuer adipiscing elit. Morbi commodo, ipsum sed pharetra gravida, orci magna rhoncus neque, id pulvinar odio lorem non turpis. Nullam sit amet enim. Suspendisse id velit vitae ligula volutpat condimentum. Aliquam erat volutpat. Sed quis velit. Nulla facilisi. Nulla libero. Vivamus pharetra posuere sapien. Nam consectetuer. Sed aliquam, nunc eget euismod ullamcorper, lectus nunc ullamcorper orci, fermentum bibendum enim nibh eget ipsum. Donec porttitor ligula eu dolor. Maecenas vitae nulla consequat libero cursus venenatis. Nam magna enim, accumsan eu, blandit sed, blandit a, eros.

0
Introduction

Part I

Preliminaries

1

The Standard Model and beyond: a theoretical overview

This is some random quote to start off the chapter.

Firstname lastname

2

The ATLAS detector and the Large Hadron Collider

2.1 The Large Hadron Collider

2.2 The ATLAS Detector

Part II

Observation and measurement of Higgs boson decays to $WW*$ with the ATLAS detector in LHC Run 1 at $\sqrt{s} = 7$ and 8 TeV

Basic research is what I am doing when I don't know what I am doing.

Wernher von Braun

3

$H \rightarrow WW^* \rightarrow \ell\nu\ell\nu$ Analysis Strategy

3.1 Introduction

This chapter will present an overview of the strategy for searching for a Higgs boson in the $H \rightarrow WW^* \rightarrow \ell\nu\ell\nu$ decay topology. Its purpose is to present in broad terms how the search and measurement are undertaken, before going into details on the specific sub-categories within the broader analysis.

First, the topology of the signal final state and corresponding backgrounds are presented. Next, an overview of the variables used to reduce the backgrounds and enhance the signal is given. These will be described in general, while specific values of selection cuts and background estimation will be provided in subsequent chapters. Finally, the parameters of interest in the search and measurement will be defined, and a brief overview of the statistical treatment of the final Higgs candidates is shown.

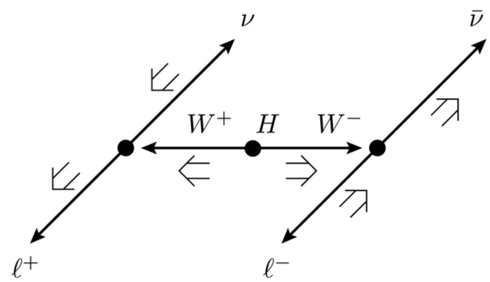

Figure 3.1: A cartoon of the WW final state. Momenta are represented with thin arrows, spins with thick arrows.[9]

3.2 Signal topology

The analysis presented here and in subsequent chapters is the study of the Higgs boson in the WW final state, where each W boson subsequently decays into a charged lepton and a neutrino. In its simplest form, the final state will then consist of two neutrinos and two charged leptons, each of which can be either an electron or a muon. If one or both of the Ws decay to τ leptons, only leptonic decays of the τ are considered, leading to additional neutrinos in the final state but still giving two charged leptons as before. Neutrinos are not detected in ATLAS, so the final state ultimately consists of two reconstructed leptons and missing transverse momentum (denoted as $E_{\mathrm{T}}^{\mathrm{miss}}$). Final states where both of the charged leptons are electrons or muons are referred to as the "same flavor" final states, while those with one electron and one muon are referred to as "different flavor".

The final state leptons will also exhibit unique correlations due to the fact that they are arising from the decay of a spin zero resonance. In particular, the spins of the final state leptons and neutrinos must all cancel, as shown in figure 3.1. Because the neutrino has a left handed helicity and the anti-neutrino has a right handed helicity, the spin and momentum of the particles will be anti-aligned and aligned, respectively. In the transverse plane, the momenta of all four final state objects must cancel as well. With the constraint of having both the momenta and the spin alignments cancel, the final state kinematics strongly prefer having a small angle between the leptons in the transverse plane (low $\Delta\phi_{\ell\ell}$). This angular correlation will also lead to low values of the di-lepton invariant mass $m_{\ell\ell}$. These unique signal final state kinematic correlations will be exploited to define the ultimate signal region.

While the basic final state consists of two leptons and $E_{\mathrm{T}}^{\mathrm{miss}}$, there can be additional objects as well depending on the production mode of the Higgs. As described in detail in Chapter 1, if the Higgs is produced via vector boson fusion production, there will be two additional forward jets in the event. Even in gluon fusion, one or more jets can be produced through initial state radiation from the incoming gluons. The analysis is separated into different signal regions depending on the number of hard jets reconstructed in the final state as well.

3.3 Background processes

Many processes from the Standard Model can also produce a final state with two leptons and missing transverse momentum . This section lists the dominant backgrounds to Higgs production. It gives general descriptions of how the backgrounds mimic Higgs production and how they can be reduced. The details of background estimation and specific cuts are left for later sections. Table3.1 summarizes the different processes.

3.3.1 Standard Model WW production

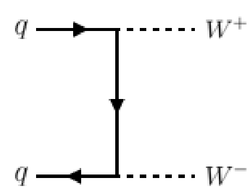

Figure 3.2: Feynman diagram for Standard Model WW production

Non-resonant Standard Model diboson production, as shown in figure 3.2, is an irreducible background to Higgs boson production in the WW final state. It produces the same exact final state objects, namely leptonically decaying W bosons. There are no additional objects in the final state that allow for background reduction. Therefore the analysis solely relies on the correlations between the leptons to reduce this background.

3.3.2 Top quark production

Production of top quarks, either in pairs ($t\bar{t}$ production) or singly (e.g. Wt production), can also mimic Higgs production. Because top quarks decay via $t \to Wb$, top pair production can produce a final state with two W bosons that then decay leptonically. In this case, however, there are two additional jets from the bottom quarks in the final state. This allows the analysis to veto on the presence of jets identified as originating from a b in order to reduce the size of the background.

Single top production can occur via s-channel, t-channel, or associated production (Wt). The mode which most closely resembles the Higgs final state is Wt. In this case, there are two real W bosons produced, as with $t\bar{t}$. However, the decay of the single top quark will still also produce one b-jet, meaning a b veto will reduce this background as well.

Figure 3.3 shows the Feynman diagrams for $t\bar{t}$ and Wt production.

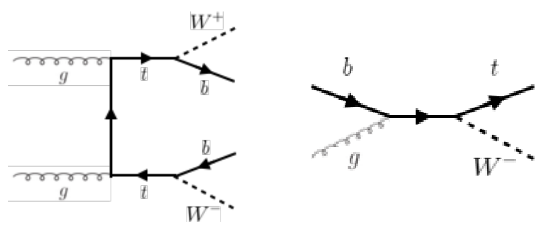

Figure 3.3: Feynman diagrams for top pair production (left) and Wt production (right)

3.3.3 W+jets background

Single W boson production, in association with jets, is a unique background. The other background considered so far have all included real leptons in the final state. In this case, however, only one real lepton from the decay of a W exists in the final state. The second reconstructed lepton can arise from two different cases. First, the lepton may truly be an algorithm "fake", or a jet misidentified as a lepton by either the electron or muon reconstruction algorithms. Second, the lepton may be a real lepton but coming from semi-leptonic decays of particles inside the shower of the jet. This background can be reduced by requiring that the reconstructed lepton have little activity surrounding it in the calorimeter (also known as an "isolated" lepton). Figure 3.4 shows the Feynman diagram for W+jets production.

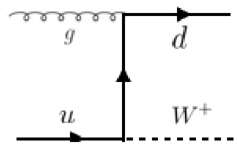

Figure 3.4: An example Feynman diagram of W+jets production

3.3.4 Z/γ^*+JETS BACKGROUND

Production of a Z/γ^* in association with jets (also known as Drell-Yan) is also a background to Higgs production. In particular, the same flavor final states have a large Z+jets background, as the Z decays into two leptons of the same flavor. (This background also enters the different flavor final state through the leptonic decays of $Z \to \tau\tau$). Figure 3.5 shows the production of a Z in association with one jet. Because there are no neutrinos in this final state, variables like $E_{\mathrm{T}}^{\mathrm{miss}}$ can be used to reduce the background.

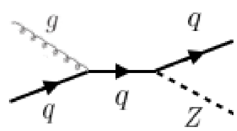

Figure 3.5: An example Feynman diagram of Z+jets production

3.3.5 OTHER (SUBDOMINANT) BACKGROUNDS

There are additional processes which contrinute to the background composition but are not produced as frequently as those listed already. The first of these are referred to as VV or "Other diboson" processes and include multiple Standard Model diboson processes, including WZ, ZZ, $W\gamma$, $W\gamma^*$, and $Z\gamma$ production. Additionally, there is background from QCD multijet production, where two jets are misidentified as leptons.

3.4 ISOLATING AN $H \to WW^* \to \ell\nu\ell\nu$ SIGNAL

As presented in section 3.2, there are many different combinations of objects that can define a $H \to WW^* \to \ell\nu\ell\nu$ final state. The multiplicity of jets and the flavor combinations of the leptons both lead to a combinatorically large number of potential signal regions. Additionally, signal regions can be optimized separately to be sensitive to the distinct production modes of the Higgs. Gluon fusion, vector

Category	Process	Description
SM WW	$WW \to \ell\nu\ell\nu$	Real leptons and neutrinos
Top quark production	$t\bar{t} \to WbW\bar{b} \to \ell\nu b\ell\nu\bar{b}$	Real leptons, untagged bs
	$tW \to WbW \to \ell\nu\ell\nu b$	Real leptons, untagged b
	$t\bar{b}$, $tq\bar{b}$	Untagged b, jet misidentified as lepton
Drell-Yan	$Z/\gamma^* \to ee, \mu\mu$	"Fake" $E_{\mathrm{T}}^{\mathrm{miss}}$
	$Z/\gamma^* \to \tau\tau \to \ell\nu\nu\ell\nu\nu$	Real leptons and neutrinos
Other dibosons	$ZZ \to \ell\ell\nu\nu$	Real leptons and neutrinos
	$W\gamma^*, WZ \to \ell\nu\ell\ell, ZZ \to \ell\ell\ell\ell$	Unreconstructed leptons
	$W\gamma, Z\gamma$	γ reconstructed as e, unreconstructed lepton
W+jets	$Wj \to \ell\nu j$	Jet reconstructed as lepton
QCD multijet	jj	Jets reconstructed as leptons

Table 3.1: A summary of backgrounds to the $H \to WW^* \to \ell\nu\ell\nu$ signal

boson fusion, and associated production of a Higgs all lead to unique final state topologies. Figure 3.6 delineates the different signal regions used in the gluon fusion and vector boson fusion $H \to WW^*$ analyses. While there are different optimizations possible in each signal region, there are also some commonly shared selections that will be described here.

3.4.1 Event pre-selection

Before being sorted into the distinct signal regions, basic cuts are applied on the reconstructed objects in the event to select Higgs-like event candidates. First, two oppositely charged leptons are required. The p_{T} threshold on the leptons is a particularly important consideration for this signal. Because the second W produced in the decay can be off-shell, it tends to produce lower momentum leptons. Thus, being able to lower the p_{T} threshold while still maintaining a low background rate is critical. Figure 3.7 shows an example of the subleading lepton p_{T} for a VBF $H \to WW^*$ signal compared to the corresponding $t\bar{t}$ background. Note that the lepton p_{T} spectrum is considerably softer in the signal sample.

Once the leptons are selected, the last requirement for event pre-selection is the presence of neutrinos. As neutrinos cannot be detected directly in ATLAS, $E_{\mathrm{T}}^{\mathrm{miss}}$ can be used as a proxy for the combined neutrino momentum in the transverse plane. In general, it is expected that the signal should have a harder

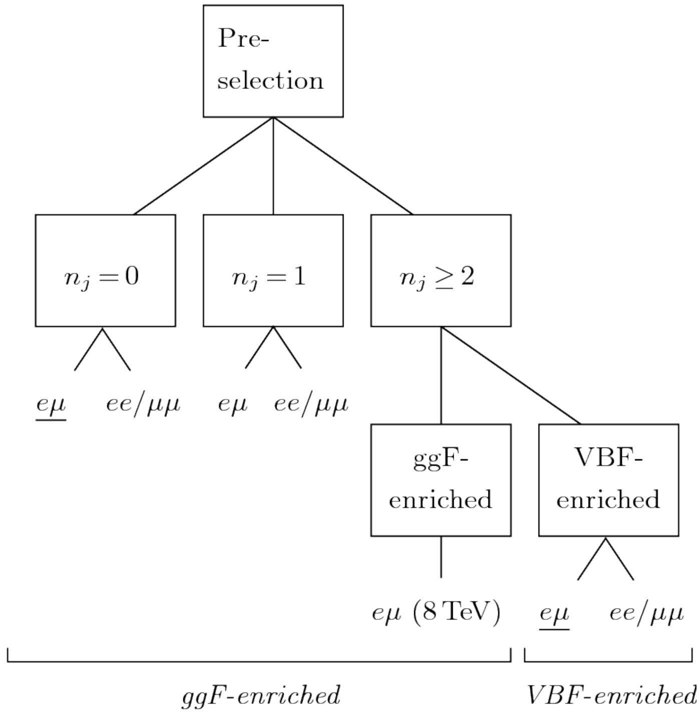

Figure 3.6: An illustration of the unique analysis signal regions [9]

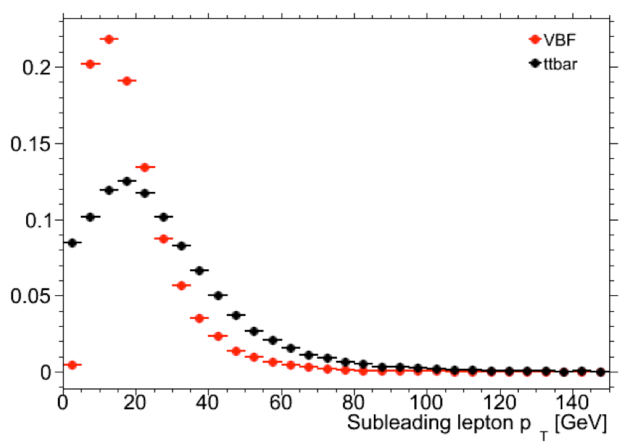

Figure 3.7: A comparison of the subleading lepton p_{T} spectrum between VBF $H \rightarrow WW^*$ production and $t\bar{t}$ background

$E_{\mathrm{T}}^{\mathrm{miss}}$ spectrum than backgrounds, especially if those backgrounds did not contain neutrinos. One additional consideration when using $E_{\mathrm{T}}^{\mathrm{miss}}$ is the fact that mis-measurements of objects in the detector can lead to imbalances in the transverse plane that are not due to real particles escaping the detector. One indicator that this is the case is that the $E_{\mathrm{T}}^{\mathrm{miss}}$ vector in the transverse plane will be pointing in the same direction as the mis-measured object. Therefore, a new variable, $E_{\mathrm{T,rel}}^{\mathrm{miss}}$, is used in the pre-selection. $E_{\mathrm{T,rel}}^{\mathrm{miss}}$ is defined in equation 3.1.

$$E_{\mathrm{T,rel}}^{\mathrm{miss}} = \begin{cases} E_{\mathrm{T}}^{\mathrm{miss}} \ \sin\Delta\phi_{\mathrm{near}} & \text{if } \Delta\phi_{\mathrm{near}} < \pi/2 \\ E_{\mathrm{T}}^{\mathrm{miss}} & \text{otherwise,} \end{cases} \tag{3.1}$$

If the closest object to the $E_{\mathrm{T}}^{\mathrm{miss}}$ vector is within $\pi/2$ radians in the transverse plane, the $E_{\mathrm{T}}^{\mathrm{miss}}$ is projected away from this object. Otherwise, the normal $E_{\mathrm{T}}^{\mathrm{miss}}$ vector is used. Figure 3.8 shows a graphical illustration of this concept.

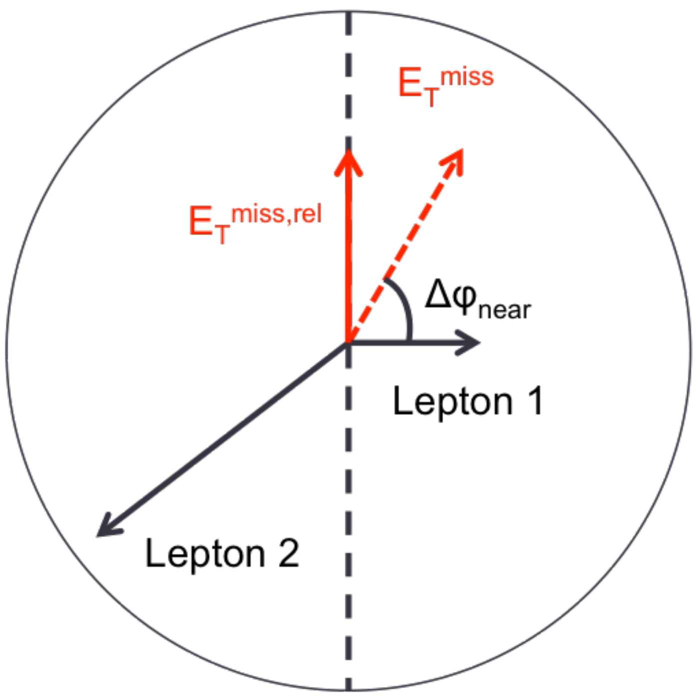

Figure 3.8: A graphical illustration of the $E_{\mathrm{T,rel}}^{\mathrm{miss}}$ calculation

Once both the lepton and $E_{\mathrm{T}}^{\mathrm{miss}}$ pre-selections are made, the analysis can be divided into different regions according to jet multiplicity.

3.4.2 Jet multiplicity

Jet multiplicity, denoted as n_j, is used to sub-divide the analysis into its distinct signal regions. The reason for this is twofold. First, different jet multiplicity bins will be more or less sensitive to different Higgs production modes. For example, the $n_j \geq 2$ region is more sensitive to VBF production because of the two hard jets produced at matrix element level. For gluon fusion production to enter this bin, two initial state radiation jets must be emitted. Second, background composition varies greatly in different bins of n_j. Figure 3.9 shows the jet multiplicity in both the different flavor and same flavor regions. It also shows the background composition in the bins of n_b. There are a few clear trends from this distribution. The first is that the Drell-Yan background dominates in the same flavor channels for $n_j \leq 1$. Second, the top background becomes a clear contributor to the total background for $n_j \geq 1$. Lastly, the SM WW production dominates in the $n_j = 0$ bin, as it is an irreducible background to $H \to WW^*$ production. Because of these distinct features, each jet multiplicity bin is treated separately.

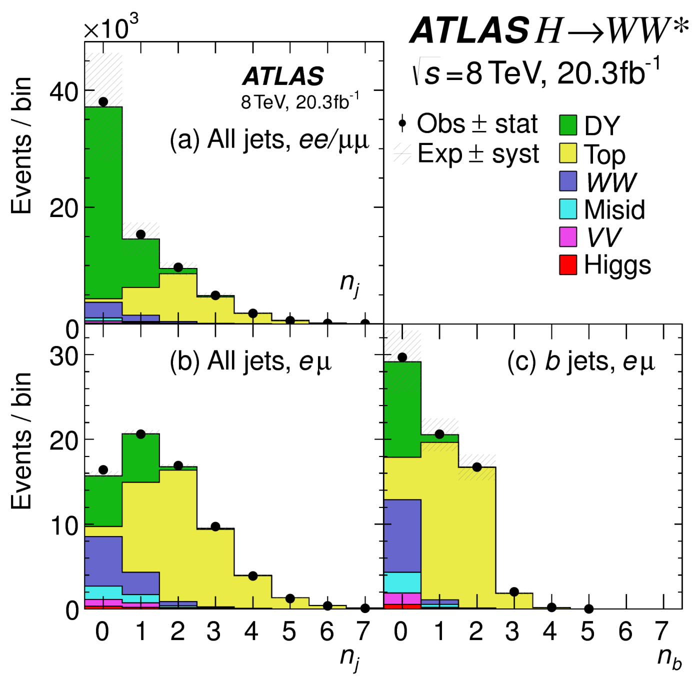

Figure 3.9: Predicted backgrounds (compared with data) as a function of n_j (a and b) and n_b (c)

3.5 Background reduction in same-flavor final states

As described in section 3.4.2, the background composition of the same flavor final states is unique to that of the different flavor states. In particular, Drell Yan processes play a much larger role because the Z/γ^* decays to same flavor leptons. Because real neutrinos are absent in the Z/γ^* decays to ee and $\mu\mu$, a cut on $E_{\mathrm{T}}^{\mathrm{miss}}$ should largely reduce the background. However, as this section will demonstrate, with increasing pileup conditions the resolution of the calorimeter-based $E_{\mathrm{T}}^{\mathrm{miss}}$ degrades greatly. Therefore, two new variables for Z/γ^* background reduction are constructed and described in this section.

3.5.1 Pileup and $E_{\mathrm{T}}^{\mathrm{miss}}$ resolution

Secondary interactions of protons in the colliding bunches of the LHC (known as pileup interactions, described in detail in Chapter 2) deposit energy into the ATLAS calorimeter on top of the energy that comes from the hard scatter process that is being searched for or analyzed. The calculation of $E_{\mathrm{T}}^{\mathrm{miss}}$ is fundamentally Poissonian, as summing up all of the energy deposits in individual calorimeter cells or clusters is similar to a counting experiment. Thus, the energy resolution scales as $\sqrt{E}$, just as the error on a mean of N in a Poisson distribution is $\sqrt{N}$. As more energy is deposited in the calorimter, the $E_{\mathrm{T}}^{\mathrm{miss}}$ resolution degrades, meaning that the $E_{\mathrm{T}}^{\mathrm{miss}}$ resolution is particularly sensitive to LHC instantaneous luminosity conditions.

Figure 3.10 shows an event display of a Z/γ^* + jets event candidate with the twenty-five reconstructed primary vertices. This display illustrates that while the interaction of interest only has tracks coming from the hardest primary vertex, all of the secondary interactions will deposit energy in the calorimeter as well.

Figure 3.11 shows the RMS of the $E_{\mathrm{T}}^{\mathrm{miss}}$ distribution in $Z \to \mu\mu$ events (where there are no real neutrinos) as a function of the number of the average number of interactions. Under 2011 LHC conditions, this RMS was approximately 9 GeV, while under 2012 running conditions the resolution worsened to 12 GeV. This worsening dilutes the efficacy of a cut on $E_{\mathrm{T}}^{\mathrm{miss}}$ to reduce the Z/γ^* background.

3.5.2 Track-based definitions of missing transverse momentum

Because the increasing number of secondary proton-proton interactions degrades calorimeter-based $E_{\mathrm{T}}^{\mathrm{miss}}$ resolution, a new variable using only contributions from the primary interaction vertex is necessary to further reduce the Z/γ^* background. While it is not possible to associate calorimeter energy deposits with a particular vertex, individual charged particle tracks in the Inner Detector are associated to

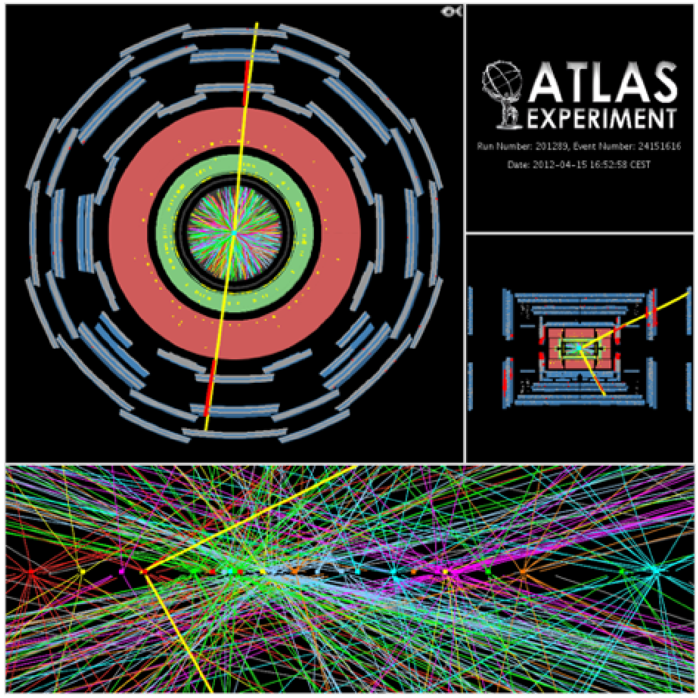

Figure 3.10: An event display of a Z/γ^* + jets event illustrating the effect of pileup interactions

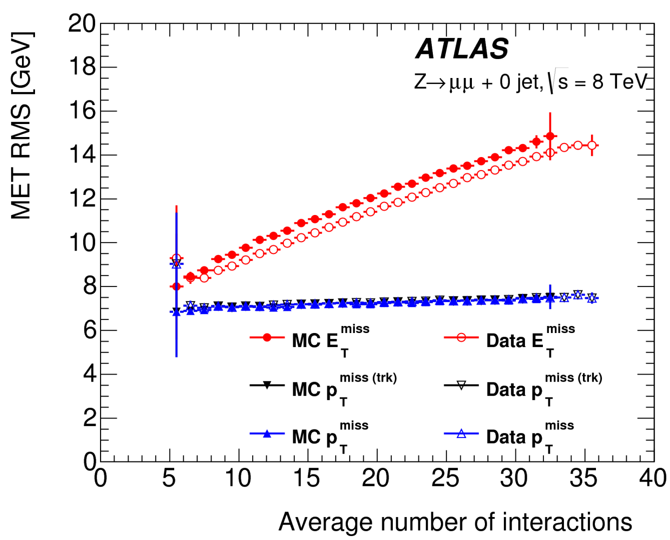

Figure 3.11: The RMS of different missing transverse momentum definitions as a function of the average number of interactions per bunch crossing

unique vertices. Thus, two track-based definitions of missing transverse momentum , using only tracks coming from the primary vertex in the event, are used in the analysis. The simplest variable, $p_{\mathrm{T}}^{\mathrm{miss\,(trk)}}$, is the vectorial sum of the p_{T} of all of the tracks from the primary vertex and the selected leptons (excluding the tracks associated with the selected leptons to avoid double counting). This is defined in equation 3.2.

$$\boldsymbol{p}_{\mathrm{T}}^{\mathrm{miss\,(trk)}} = -\Bigg(\sum_{\substack{\text{selected}\\\text{leptons}}} \boldsymbol{p}_{\mathrm{T}} + \sum_{\substack{\text{other}\\\text{tracks}}} \boldsymbol{p}_{\mathrm{T}}\Bigg), \tag{3.2}$$

In events with hard jets, a better resolution on the missing transverse momentum is obtained by including the calorimeter based measurement of the hard jets rather than the track based measurements. Thus, another variable, $p_{\mathrm{T}}^{\mathrm{miss}}$, is defined, using the nominal measurements of p_{T} for the selected leptons and jets and using tracks rather than calorimeter clusters for the soft component of the missing transverse momentum . This is defined in equation 3.3.

$$\boldsymbol{p}_{\mathrm{T}}^{\mathrm{miss}} = -\Bigg(\sum_{\substack{\text{selected}\\\text{leptons}}} \boldsymbol{p}_{\mathrm{T}} + \sum_{\substack{\text{selected}\\\text{jets}}} \boldsymbol{p}_{\mathrm{T}} + \sum_{\substack{\text{other}\\\text{tracks}}} \boldsymbol{p}_{\mathrm{T}}\Bigg), \tag{3.3}$$

Figure 3.11 illustrates that these two new variables accomplish their intended purpose. The resolution as a function of mean number of interactions for both $p_{\mathrm{T}}^{\mathrm{miss\,(trk)}}$ and $p_{\mathrm{T}}^{\mathrm{miss}}$ is much flatter compared to the dependence for $E_{\mathrm{T}}^{\mathrm{miss}}$.

Figure 3.12a shows the difference between the true and reconstructed values of missing transverse momentum using both the track-based $p_{\mathrm{T}}^{\mathrm{miss}}$ and calorimeter based $E_{\mathrm{T}}^{\mathrm{miss}}$. The RMS of the distribution improves by 3.5 GeVwhen using $p_{\mathrm{T}}^{\mathrm{miss}}$.

3.5.3 Distinguishing Z/γ^* +jets and $H \to WW^*$ topologies

The track-based definitions of missing transverse momentum were constructed to mitigate degrading performance as a function of pileup. However, an additional variable can be constructed to exploit kinematic and topological differences between the Z/γ^* background and $H \to WW^*$ signal. Because there are no real neutrinos in the final state (in the case of $Z/\gamma^* \to ee, \mu\mu$ decays), the dilepton system of a Z/γ^* will be balanced with the jets produced in the hard scatter. A new variable, f_{recoil}, is constructed to estimate the balance between the dilepton system and the jets in the quadrant opposite the dilepton vector in the transverse plane. It is defined in equation 3.4. The numerator of f_{recoil} is the magnitude of

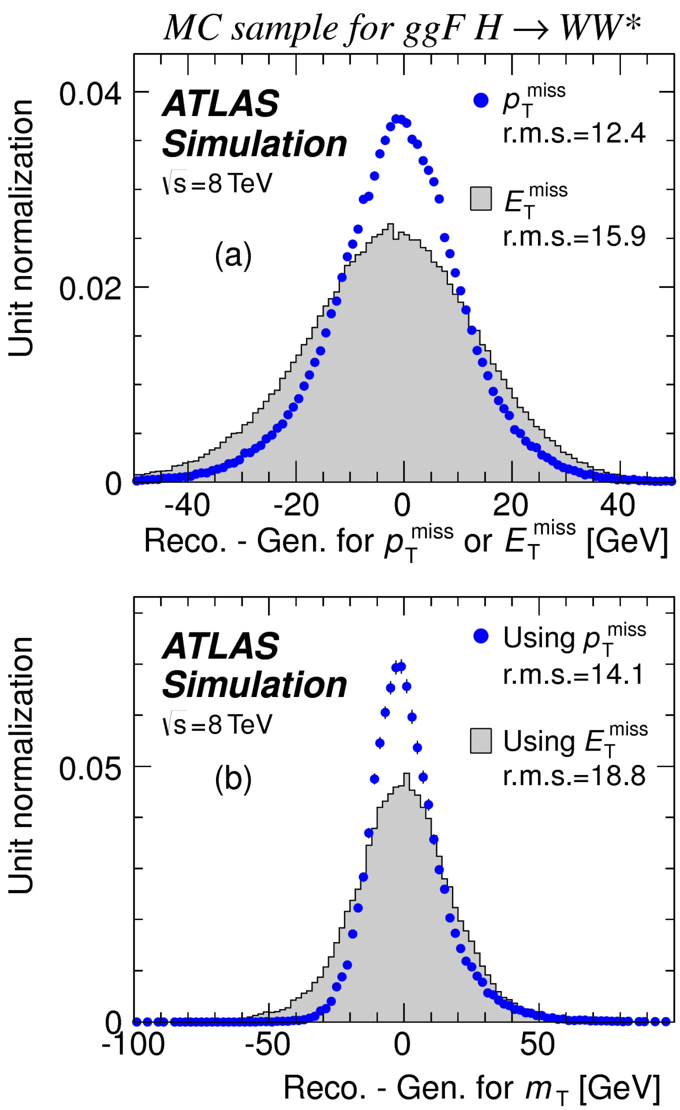

Figure 3.12: The difference between the true and reconstructed values of the missing transverse momentum (a) and m_{T} (b) in a gluon fusion signal sample

the vectorial sum of the p_{T} of jets in the quadrant opposite the dilepton system, weighted by each jet's Jet Vertex Fraction (JVF, described in chapter 2). The denominator is the magnitude of the dilepton p_{T}.

$$f_{\mathrm{recoil}} = \left| \sum_{\mathrm{jets}\ j\ \mathrm{in}\ \wedge} \mathrm{JVF}_j \cdot \boldsymbol{p}_{\mathrm{T}}^{j} \right| \Big/ p_{\mathrm{T}}^{\ell\ell}. \tag{3.4}$$

Figure 3.13 shows a shape comparison of the distribution of f_{recoil} in a simulated $Z/\gamma^* + \mathrm{jets}$ sample, a $H \to WW^*$ signal sample, and other backgrounds that contain real neutrinos. The Z/γ^* + jets events tend to be more balanced between the dilepton system and recoiling jets, while the processes containing real neutrinos are less balanced in the transverse plane. Thus, a cut on f_{recoil} will also reduce the Z/γ^* + jets background while maintaining a good signal efficiency.

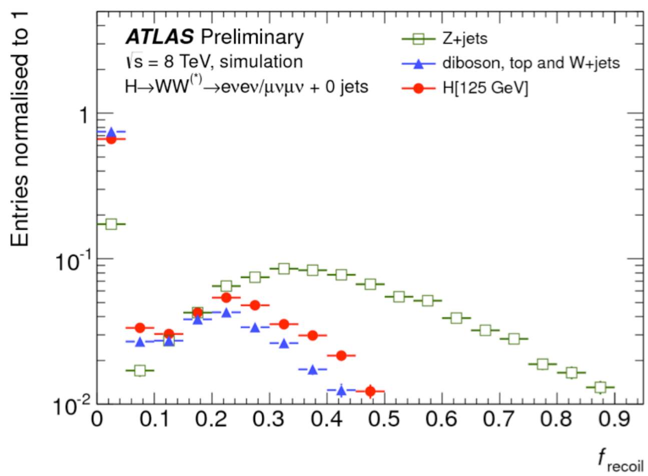

Figure 3.13: Comparison of f_{recoil} distributions for Z/γ^*+jets, $H \to WW^*$, and other backgrounds with real neutrinos.

3.5.4 Optimizing background reduction cuts

The cuts on $p_{\text{T}}^{\text{miss (trk)}}$ and f_{recoil} used to reduce the Z+jets background must be optimized to maximize their efficacy. Figure 3.14 shows an early attempt to optimize the combination of the two cuts in the gluon fusion zero jet bin. Each bin shows the expected signal significance if the $p_{\text{T,rel}}^{\text{miss (trk)}}$ is required to be greater than the left edge of the bin and the f_{recoil} is required to be less than the top edge of the bin. The figure shows that the best signal significance comes from requiring low values of f_{recoil} (< 0.05) and $p_{\text{T,rel}}^{\text{miss (trk)}}$ values greater than 45 GeV.

3.6 Parameters of interest and statistical treatment

As with any search or measurement, there are particular parameters of the Higgs that the $H \to WW^*$ analysis is interested in measuring. In this case, the parameters of interest are the mass of the Higgs boson and its production cross section. Because the $H \to WW^* \to \ell\nu\ell\nu$ process does not have a closed

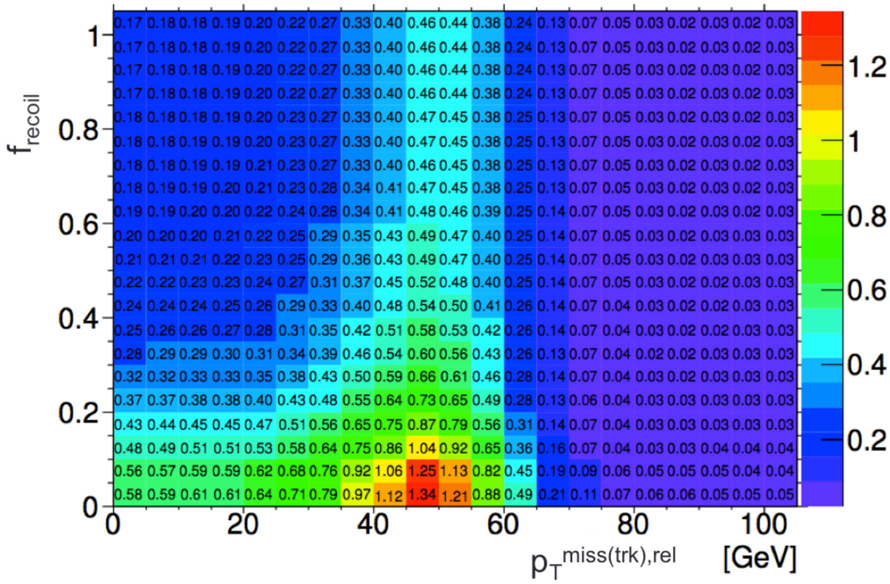

Figure 3.14: Signal significance as a function of cut value in the ggF $H \to WW^*$ with $n_j = 0$

final state, it is not possible to measure the full invariant mass of the particle that may have produced the final state. However, a proxy for the invariant mass using transverse plane information can be defined. This is described in more detail in section 3.6.1. The second parameter of interest is the ratio of the measured cross section to that expected from the Standard Model Higgs, which is denoted a μ. This is defined in equation 3.5.

$$\mu = \frac{\sigma}{\sigma_{\text{SM}}} \tag{3.5}$$

All of the likelihoods used in the statistical analysis of the final signal region events are paramaterized as a function of μ. μ is a natural variable for hypothesis testing, as $\mu = 0$ corresponds to a background only hypothesis and $\mu = 1$ corresponds exactly to a Standard Model Higgs.

3.6.1 Transverse mass

Because the longitudinal information about the neutrinos is not attainable, the $H \to WW^* \to \ell\nu\ell\nu$ analysis uses a mass variable, the transverse mass, that exploits information in the transverse plane as a proxy for the full invariant mass. The transverse mass is defined in equation 3.6.

$$m_{\mathrm{T}} = \sqrt{\left(E_{\mathrm{T}}^{\ell\ell} + p_{\mathrm{T}}^{\mathrm{miss}}\right)^2 - \left|\,\boldsymbol{p}_{\mathrm{T}}^{\ell\ell} + \boldsymbol{p}_{\mathrm{T}}^{\mathrm{miss}}\,\right|^2}, \tag{3.6}$$

Here the $E_{\mathrm{T}}^{\ell\ell}$ and $p_{\mathrm{T}}^{\ell\ell}$ are the transverse energy and momentum of the dilepton system, while $p_{\mathrm{T}}^{\mathrm{miss}}$ is a proxy for the transverse momentum of the di-neutrino system. The track-based $p_{\mathrm{T}}^{\mathrm{miss}}$ is used in the m_{T} rather than the calorimeter based $E_{\mathrm{T}}^{\mathrm{miss}}$ because it has a better resolution on the true transverse mass. Figure 3.12b shows the improvement in the RMS of the difference between the true and reconstructed transverse mass in a ggF signal sample. The RMS improves by 4.7 GeVusing $p_{\mathrm{T}}^{\mathrm{miss}}$ in the m_{T} calculation.

3.6.2 Statistical treatment*

Likelihood function

The statistical analysis of final event candidates is framed as a hypothesis test, where the null hypothesis is background-only (no Standard Model Higgs). The first step in the analysis is to form a likelihood function for the data. In its simplest form, this likelihood is the probability of observing the number of events seen in the final signal region given knowledge of the signal strength. Because observation of events is fundamentally a Poisson counting experiment, this simple likelihood can be expressed as a Poisson probability of observing N events given a total number of predicted signal and background events. This basic likelihood is shown in equation 3.7.

$$\mathcal{L}(\mu) = P\left(N|\mu S + B\right) \tag{3.7}$$

Here, P is the Poisson probability density function, N is the total number of observed events, μ is the signal strength, S is the predicted number of signal events, and B is the predicted number of background events.

In particle physics, certain background estimates are commonly normalized in so-called "control" re-

*Many thanks to Aaron Armbruster, whose thesis [4] inspired parts of this section.

gions and those predictions are scaled by the same normalization factor in the signal region. This leads to a slightly more complicated likelihood, which is a function of both the signal strength and the background normalization. This is shown in equation 3.8.

$$\mathcal{L}(\mu, \theta) = P\left(N|\mu S + \theta B\right) P\left(N_{\mathrm{CR}}|\theta B_{\mathrm{CR}}\right) \tag{3.8}$$

Here, θ is a so-called "nuisance parameter", a parameter that is not a primary parameter of interest but still enters the likelihood. The second Poisson term adds an extra term to the likelihood, enforcing the fact that the background normalization must be consistent with the number of observed events in data in the control region, N_{CR}.

So far, these two formulations of likelihoods have assumed a single signal region and do not take into account any shape information of potential discriminating variables. The $H \to WW^*$ analysis is divided into many different categories, and we can perform the same counting experiment described above in each individual category. As mentioned in section 3.6.1, the transverse mass is used as the primary discriminating variable in many of the $H \to WW^*$ sub-analyses, so additionally we can perform the same counting experiment in each bin of the m_{T} distribution to incorporate some shape information. Thus, the total likelihood becomes a product over signal regions and bins of the m_{T} distribution. Finally, there are usually many backgrounds that are normalized in control regions, so the new formulation of the likelihood takes this into account as well by including a product over control regions in the second Poisson term. All of these modifications are shown in equation 3.9.

$$\mathcal{L}\left(\mu, \boldsymbol{\theta}\right) = \prod_{\substack{\mathrm{SRs\,i} \\ \mathrm{bins\,b}}} P\left(N_{ib} \middle| \mu S_{ib} + \sum_{\mathrm{bkg\,k}} \theta_k B_{kib}\right) \prod_{\mathrm{CRs\,l}} P\left(N_l \middle| \sum_{\mathrm{bkg\,k}} \theta_k B_{kl}\right) \tag{3.9}$$

The final step to get the full likelihood used in the analysis is to add nuisance parameters for the systematic uncertainties. In cases where the uncertainty does not affect the shape of m_{T} bin-by-bin, each systematic uncertainty ϵ is allowed to affect the expected event yields through a linear response function of the nuisance parameter, namely $\nu(\theta) = (1 + \epsilon)^{\theta}$. If instead the uncertainty does affect the shape, the effect is instead parameterized by $\nu_b(\theta) = 1 + \epsilon_b \theta$. The value of the nuisance parameters for the systematic uncertainty are constrained with a Gaussian term that is added to the likelihood as well. This is of the form $g(\delta|\theta) = e^{-(\delta-\theta)^2/2}/\sqrt{2\pi}$, where δ is the central value and θ is a nuisance parameter. Finally, a last term is added to account for the statistical uncertainty in the Monte Carlo samples used, which adds an additional poisson term. The full likelihood used in the final statistical analysis is defined in equation 3.10.

$$\begin{aligned}\mathcal{L}(\mu,\boldsymbol{\theta}) = &\prod_{\substack{\text{SRs i}\\ \text{bins b}}} P\left(N_{ib}\middle|\mu S_{ib}\cdot\prod_{\substack{\text{sig.}\\ \text{syst.}\\ r}}\nu_{br}(\theta_r)+\sum_{\text{bkg k}}\theta_k B_{kib}\cdot\prod_{\substack{\text{bkg.}\\ \text{syst.}\\ s}}\nu_{bs}(\theta_s)\right)\\ &\cdot\prod_{\text{CRs l}} P\left(N_l\middle|\sum_{\text{bkg k}}\theta_k B_{kl}\right)\\ &\cdot\prod_{\substack{\text{syst}\\ t}} g(\delta_t|\theta_t)\cdot\prod_{\text{bkg k}} P(\xi_k|\zeta_k\theta_k)\end{aligned}\tag{3.10}$$

In the fourth term of the equation, quantifying uncertainty due to finite Monte Carlo sample size, ξ represents the central value of the background prediction, θ is the associated nuisance parameter, $\zeta = (B/\delta B)^2$, where δB is the statistical uncertainty of B.

The best fit value of the signal strength μ is determined by finding the values of μ and $\boldsymbol{\theta}$ that maximize the likelihood, while setting $\delta = 0$ and $\xi = \zeta$.

Once the likelihood is defined, a test statistic must be built for use in hypothesis testing.

Test statistic

To distinguish whether the data match a background only or background and signal hypothesis, a test statistic must be used. The $H \to WW^*$ analysis used the profile likelihood technique[11]. The first step in formulating this test statistic is to define the profile likelihood ratio, shown in equation 3.11.

$$\lambda(\mu) = \frac{\mathcal{L}\left(\mu,\hat{\hat{\theta}}_\mu\right)}{\mathcal{L}\left(\hat{\mu},\hat{\theta}\right)}\tag{3.11}$$

Here $\hat{\hat{\theta}}_\mu$ is the value of θ that maximizes the likelihood for the choice of μ being tested. Additionally,

$\hat{\theta}$ and $\hat{\mu}$ represent the values of θ and μ that gives the overall maximum value of the likelihood.

Once this is defined, a test statistic q_μ is constructed. This is shown in equation 3.12.

$$q_\mu = -2 \ln \lambda(\mu) \tag{3.12}$$

A higher value of q_μ means that the data are more incompatible with the hypothesized value of μ, and q_0 then corresponds to the value of the test statistic for the background only hypothesis. A p_0 value is then defined to quantify the compatibility between the data and the null hypothesis. The p_0 value is the probability of obtaining a value of q_0 larger than the observed value, and this is shown in equation 3.13.

$$p_0 = \int_{q_0^{\mathrm{obs}}}^{\infty} f(q_\mu|\mu = 0) dq_\mu \tag{3.13}$$

Here $f(q_\mu)$ is the probability distribution function of the test statistic. Finally, the p_0 value can be converted into a signal significance, using the formula in equation3.14, or the one-sided tail of the Gaussian distribution.

$$Z_0 = \sqrt{2}\mathrm{erf}^{-1}(1 - 2p_0) \tag{3.14}$$

The threshold for discovery used in particle physics is $Z_0 \geq 5$, more commonly known as a value of 5σ.

4

The discovery of the Higgs boson and the role of the $H \to WW^* \to \ell\nu\ell\nu$ channel

The imagination of nature is far, far greater than the imagination of man.

Richard Feynman

5 Observation of Vector Boson Fusion production of $H \to WW^* \to \ell\nu\ell\nu$

5.1 Introduction

After the discovery of a particle consistent with the Higgs boson, the $H \to WW^*$ analysis had two main goals. The first goal was to increase the sensitivity of the analysis to fully confirm that the $H \to WW^*$ process did indeed exist. The second goal was to characterize the particle as much as possible, including searching for the lower cross-section production modes, in order to confirm that it was indeed a Higgs boson. This chapter presents a dedicated search for Vector Boson Fusion (VBF) production of a Higgs boson decaying via the $H \to WW^* \to \ell\nu\ell\nu$ mode. First, basics of the topology of VBF production are presented. Then, the details of the analysis are shown, including signal region definition, background estimation techniques, and systematic uncertainties. Finally, the results of the analysis are shown. As will

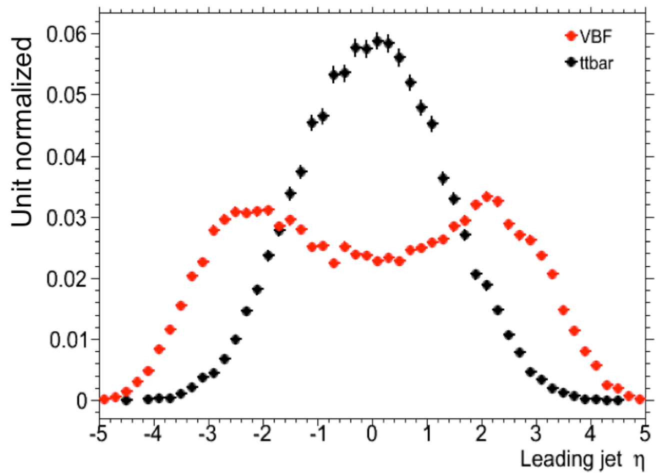

Figure 5.1: Leading jet η in VBF $H \to WW^*$ (red) and $t\bar{t}$ (black)

be shown, this analysis is the first and most sensitive observation of the VBF production mode of the Higgs on ATLAS.

5.2 Topology of VBF $H \to WW^*$ production

As discussed in Chapter 1, the characteristic feature of VBF production of the Higgs is the presence of two additional forward jets coming from the incoming partons which radiate the vector bosons that make the Higgs. These jets are forward because the outgoing partons still carry the longitudinal momentum of the incoming partons. Figure 5.1 shows the distribution of the η for the leading jet in a VBF event compared to a background top pair production event. As can be seen, the VBF jets tend to be more forward in η, while the $t\bar{t}$ jets are more central.

Because the cross section for VBF production is about an order of magnitude smaller than gluon fusion production, these forward jets must be used in order to better reduce background and achieve a good signal to background ratio. The analysis selection is constructed to maximally exploit the features of the unique VBF topology.

5.3 Data and simulation samples

The results presented here are with 20.3 fb^{-1}taken at $\sqrt{s} = 8$ TeV and 4.5 fb^{-1}taken at $\sqrt{s} = 7$ TeV. The details of the LHC and detector conditions during this period are given in Chapter 2. The trigger selection defining the dataset is discussed in section 5.3.1. The simulation samples used for signal and background modeling are given in section 5.3.2.

5.3.1 Triggers

The analysis uses a combination of single lepton and dilepton triggers to allow lowering of the p_{T} thresholds and increased signal acceptance. As discussed in Chapter 2, there are multiple levels in the ATLAS trigger system, and there are different p_{T} thresholds imposed for the leptons at each level. Additionally, some triggers have a loose selection on the isolation of the lepton (looser than that applied offline in the analysis object selection). Table 5.1 shows the thresholds used for single lepton triggers, while table 5.2 shows the thresholds coming from di-lepton triggers. The single lepton trigger efficiency for muons that pass the analysis object selection is 70% for muons in the barrel region ($|\eta| < 1.05$) and 90% in the end-cap region. The electron trigger efficiency increases with electron p_{T} but the average is approximately 90%. These efficiencies are measured by combined performance and trigger signature groups[7,8].

	Level-1 threshold	High-level threshold
Electron	18 30	$24i$ 60
Muon	15	$24i$ 36

Table 5.1: Single lepton triggers used for electrons and muons. A logical "or" of the triggers listed for each lepton type is taken. Units are in GeV, and the i denotes an isolation requirement in the trigger.

The combination of all triggers shown gives good efficiency for signal events. This efficiency is summarized in table 5.3. The relative improvement in efficiency by adding the dilepton triggers is also shown in the same table. The largest gain comes in the $\mu\mu$ channel. Overall the trigger selection shows a good efficiency for $H \to WW^*$ signal events.

	Level-1 threshold	High-level threshold
ee	10 and 10	12 and 12
$\mu\mu$	15	18 and 8
$e\mu$	10 and 6	12 and 8

Table 5.2: Di-lepton triggers used for different flavor combinations. The two thresholds listed refer to leading and sub-leading leptons, respectively. The di-muon trigger only requires a single lepton at level-1.

Channel	Trigger efficiency	Gain from 2ℓ trigger
ee	97%	9.1%
$\mu\mu$	89%	18.5%
$e\mu$	95%	8.3%
μe	81%	8.2%

Table 5.3: Trigger efficiency for signal events and relative gain of adding a dilepton trigger on top of the single lepton trigger selection. The first lepton is the leading, while the second is the sub-leading. Efficiencies shown here are for the ggF signal in the $n_j = 0$ category but are comparable for the VBF signal.

5.3.2 Monte Carlo samples

Modeling of signal and background processes in the signal region, in particular for the m_T distribution, is an important consideration for the final interpretation of the analysis. Therefore, careful consideration must be paid to which Monte Carlo (MC) generators are used for specific processes. With the exception of the W+jet and multijet backgrounds, the m_T shape used as the final discriminant is taken from simulation. (Many backgrounds are normalized from data, as described in section 5.6).

Table 5.4 shows the MC generators used for the signal and background processes, as well as their cross sections. In order to include corrections up to next-to-leading order (NLO) in the QCD coupling constant α_s, the POWHEG[16] generator is often used. In some cases, only leading order generators like ACERMC[5] and GG2VV[14] are available for the process in question. If the process requires good modeling for very high parton multiplicities, the SHERPA[13] and ALPGEN[15] generators are used to provide merged calculations for five or fewer additional partons. These matrix element level calculations must then be additionally matched to models of the underlying event, hadronization, and parton shower. There are four possible generators for this: SHERPA , PYTHIA 6[20], PYTHIA 8[21], or HERWIG[10] + JIMMY[6]. The simulation additionally requires an input parton distribution function (PDF). The CT10[12] PDFs are used for SHERPA and POWHEG simulated samples, while CTEQ6L1[17] is used for ALPGEN +HERWIG and ACERMC

Process		MC generator	$\sigma \cdot \mathcal{B}$ (pb)
Signal			
ggF	$H \to WW^*$	POWHEG +PYTHIA 8	0.435
VBF	$H \to WW^*$	POWHEG +PYTHIA 8	0.0356
VH	$H \to WW^*$	PYTHIA 8	0.0253
WW			
$q\bar{q} \to WW$ and $qg \to WW$		POWHEG +PYTHIA 6	5.68
$gg \to WW$		GG2VV +HERWIG	0.196
$(q\bar{q} \to W) + (q\bar{q} \to W)$		PYTHIA 8	0.480
$q\bar{q} \to WW$		SHERPA	5.68
VBS $WW + 2$ jets		SHERPA	0.0397
Top quarks			
$t\bar{t}$		POWHEG +PYTHIA 6	26.6
Wt		POWHEG +PYTHIA 6	2.35
$tq\bar{b}$		ACERMC +PYTHIA 6	28.4
$t\bar{b}$		POWHEG +PYTHIA 6	1.82
Other dibosons (VV)			
$W\gamma$	($p_{\mathrm{T}}^{\gamma} > 8$ GeV)	ALPGEN +HERWIG	369
$W\gamma^*$	($m_{\ell\ell} \leq 7$ GeV)	SHERPA	12.2
WZ	($m_{\ell\ell} > 7$ GeV)	POWHEG +PYTHIA 8	12.7
VBS $WZ + 2$ jets	($m_{\ell\ell} > 7$ GeV)	SHERPA	0.0126
$Z\gamma$	($p_{\mathrm{T}}^{\gamma} > 8$ GeV)	SHERPA	163
$Z\gamma^*$	(min. $m_{\ell\ell} \leq 4$ GeV)	SHERPA	7.31
ZZ	($m_{\ell\ell} > 4$ GeV)	POWHEG +PYTHIA 8	0.733
$ZZ \to \ell\ell\,\nu\nu$ ($m_{\ell\ell} > 4$ GeV)		POWHEG +PYTHIA 8	0.504
Drell-Yan			
Z	($m_{\ell\ell} > 10$ GeV)	ALPGEN +HERWIG	16500
VBF $Z + 2$ jets	($m_{\ell\ell} > 7$ GeV)	SHERPA	5.36

Table 5.4: Monte Carlo samples used to model the signal and background processes [9].

simulations. The Drell-Yan samples are reweighted to the MRST [19] PDFs, as these are found to give the best agreement between data and simulation.

Once the basic hard scattering process is simulated, it must be passed through a detector simulation and additional pile-up events must be overlaid. The pile-up events are modeled with PYTHIA 8, and the ATLAS detector is simulated with GEANT4[18]. Because of the unique phase space of the $H \to WW^*$ analysis, events are sometimes filtered at generator level to allow for more efficient generation of relevant events. The efficiency of the trigger in MC simulation does not always match the measured efficiency in data, so trigger scale factors are applied to correct the MC efficiency to the data. These are derived by the combined performance groups[7,8].

5.4 Object selection

In order to define the signal region, the analysis must first select the objects to be considered. The details of the object reconstruction algorithms are discussed in Chapter 2, while this section gives specific selection cuts used in the $H \to WW^*$ analysis.

The first step in this process is to select a primary vertex candidates. The event's primary vertex is the vertex with the largest sum of p_{T}^2 for associated tracks and is required to have at least three tracks with $p_{\mathrm{T}} > 450$ MeV. Many of the object selection cuts are then made relative to this chosen primary vertex.

5.4.1 Muons

The analysis uses combined muon candidates, where a track in the Inner Detector has been matched to a standalone track in the Muon Spectrometer. The track parameters are combined statistically in the muon reconstruction algorithm[3]. The muons are required to be within $|\eta| < 2.5$ and have a $p_{\mathrm{T}} > 10$ GeV. To reduce backgrounds coming from mis-reconstructed leptons, there are requirements on the impact parameter of the muon relative to the primary vertex. The transverse impact parameter d_0 is required to be small relative to its estimated uncertainty, the exact cut value being $d_0/\sigma_{d_0} < 3$. The longitudinal impact parameter z_0 must satisfy $|z_0 \sin\theta| < 1$ mm.

As discussed previously, the muons must also be isolated. There are two types of lepton isolations that are calculated: track-based and calorimeter-based. For muons, the track-based isolation is defined using the scalar sum $\sum p_{\mathrm{T}}$ for tracks with $p_{\mathrm{T}} > 1$ GeV (excluding the muon's track) within a cone of $\Delta R = 0.3\,(0.4)$ for muon with $p_{\mathrm{T}} > 15$ GeV ($10 < p_{\mathrm{T}} < 15$ GeV). The final isolation requirement is made my requiring that this scalar sum be no more than a certain fraction of the muon's p_{T}. This requirement varies with muon p_{T} and the exact cuts are defined in table 5.5.

The calorimeter-based muon isolation is defined using as a $\sum E_T$ calculated from calorimeter cells using the same cone size as the track-based isolation but excluding cells with $\Delta R < 0.05$ around the muon. This requirement is also definedas a cut on the ratio of the sum to the muon p_{T} and varies with muon p_{T}. The cut values are also given in table 5.5.

The isolation requirements loosen as a function of p_{T} to allow for larger signal acceptance. At low p_{T}, the isolation is tightened to reduce the W+jets background which arises from a misidentified lepton.

p_T range (GeV)	Calorimeter isolation	Track isolation
$10-15$	0.06	0.06
$15-20$	0.12	0.08
$20-25$	0.18	0.12
>25	0.30	0.12

Table 5.5: p_{T} dependent isolation requirements for muons. Muons are required to have the amount of calorimeter or track based cone sums be less than this fraction of their p_{T}.

5.4.2 Electrons

Electrons are identified by matching reconstructed clusters in the electromagnetic calorimeter with tracks in the inner detector. The electrons are identified using a likehood based method[2,1] which takes into account the shower shapes in the calorimeter, the matching of tracks to clusters, and the amount of transition radiation in the TRT. The electrons are required to have $|\eta| < 2.47$, and candidates in the transition region between the barrel and endcap ($1.37 < |\eta| < 1.52$) are excluded. As the muons, the electrons are required to have transverse impact parameter significance < 3, while in the longitudinal direction they must have $|z_0 \sin\theta| < 0.4$ mm. Some electron requirements also vary with electron E_T, and these requirements are summarized in table 5.6.

The isolation for electrons are defined similarly to the muons but with unique cuts on the objects included. The track-based isolation is defined using tracks with $p_{\mathrm{T}} > 400\,\mathrm{MeV}$ with cone sizes as defined previously. The calorimeter-based isolation also uses the same cone size as the muon, but here the cells within a 0.125×0.175 area in $\eta \times \phi$ around the electron cluster's barycenter are excluded. The other difference with respect to muons is that the denominator of the isolation ratio is the electron's E_T rather than p_{T}. The isolation cuts very with electron $E_T$and are defined in table 5.6.

The electron is also required to not be consistent with a vertex coming from a photon conversion.

p_T range (GeV)	Quality cut	Calorimeter isolation	Track isolation
$10 - 15$	Very tight LH	0.20	0.06
$15 - 20$	Very tight LH	0.24	0.08
$20 - 25$	Very tight LH	0.28	0.10
> 25	Medium	0.28	0.10

Table 5.6: p_{T} dependent requirements for electrons. Electrons are required to have the amount of calorimeter or track based cone sums be less than this fraction of their E_T.

5.4.3 Jets

Jets are clustered with the anti-k_T reconstruction algorithm using a radius parameter of $R = 0.4$. They are required to have a jet vertex fraction (JVF) of at least 50%, meaning that half of the tracks associated with the jet originated from the primary vertex. Jets with no tracks associated (i.e. those outside the acceptance of the ID) do not have this requirement applied. Jets are required to have $p_T > 25$ GeV if they are within the tracking acceptance ($|\eta| < 2.4$). Jets with $2.4 < |eta| < 4.5$ are required to have $p_{\mathrm{T}} > 30$ GeV. This tighter requirement reduces jets from pileup in the region where JVFrequirements cannot be applied. The two highest p_{T} jets in the event are referred to as the "VBF" jets and used to compute various analysis selections later.

Identification of b-jets is done using the MV1 algorithm and is limited to the acceptance of the ID ($|\eta| < 2.5$). The operating point of MV1 that is used is the one that is 85% efficient for identifying true b-jets. This operating point has a 10.3% of mis-tagging a light quark jet as a b-jet. In order to improve the rejection of b-jets, a lower threshold than the nominal p_{T} threshold described above is used. For the purposes of counting the number of b-jets, jets with p_{T} down to 20 GeVare used.

5.4.4 Overlap removal

There are some cases where certain reconstructed objects will overlap and one will have to be chosen (for example, an electron and a jet in the calorimeter). First, the case of lepton overlap is dealt with. If an electron candidate extends into the muon spectrometer, it is removed. If a muon or electron have a $\Delta R < 0.1$, the electron is removed and the muon is kept. If two electron candidates overlap within the same radius, then the higher E_T electron is kept. Next, the overlap between leptons and jets is considered. If an electron and jet are within $\Delta R < 0.3$ of one another, the electron is kept and the jet is removed. However, if a muon and jet overlap within $\Delta R < 0.3$, the jet is kept (as it is likely that the muon is the result of a semileptonic decay inside the jet).

Once the overlap removal is complete, the final set of objects used in the analysis is defined.

5.5 Analysis selection

5.6 Background estimation

5.7 Systematic uncertainties

5.8 Results

6

Combined Run 1 $H \to WW^* \to \ell\nu\ell\nu$ results

Part III

Search for Higgs pair production in the $HH \to b\bar{b}b\bar{b}$ channel in LHC Run 2 at $\sqrt{s} =$ 13 TeV

7

Search overview

8

Search for Higgs pair production in boosted final states

9

Results with Run 2 2015 dataset

Part IV

Looking ahead

10

Conclusion

We found the Higgs. Then measured it. Then used it to look for new physics. What a time to be alive!

References

[1] (2012). *Improved electron reconstruction in ATLAS using the Gaussian Sum Filter-based model for bremsstrahlung*. Technical Report ATLAS-CONF-2012-047, CERN, Geneva.

[2] (2014). *Electron efficiency measurements with the ATLAS detector using the 2012 LHC proton-proton collision data*. Technical Report ATLAS-CONF-2014-032, CERN, Geneva.

[3] Aad, G. et al. (2014). Measurement of the muon reconstruction performance of the ATLAS detector using 2011 and 2012 LHC proton–proton collision data. *Eur. Phys. J.*, C74(11), 3130.

[4] Armbruster, A. J. (2013). Discovery of a higgs boson with the atlas detector. CERN-THESIS-2013-047.

[5] B. P. Kersevan and E. Richter-Was (2004). The Monte Carlo event generator AcerMC version 2.0 with interfaces to PYTHIA 6.2 and HERWIG 6.5.

[6] Butterworth, J. M., Forshaw, J. R., & Seymour, M. H. (1996). Multiparton interactions in photoproduction at HERA. *Z. Phys.*, C 72, 637.

[7] Collaboration, A. (2014). Performance of the ATLAS muon trigger in pp collisions at $\sqrt{s}$ =8 TeV. *Eur. Phys. J. C*, (arXiv:1408.3179. CERN-PH-EP-2014-154), 75. 19 p.

[8] collaboration, A. (2015). Electron trigger performance in 2012 ATLAS data. ATLAS-COM-DAQ-2015-091.

[9] Collaboration, A. (2015). Observation and measurement of higgs boson decays to ww* with the atlas detector. *Phys. Rev. D*, 92(012006).

[10] Corcella, G. et al. (2001). HERWIG 6: An event generator for hadron emission reactions with interfering gluons (including super-symmetric processes) . *JHEP*, 01, 010.

[11] G. Cowan, K. Cranmer, E. Gross, and O. Vitells (2011). Asymptotic formulae for likelihood-based tests of new physics. *Eur. Phys. J.*, C 71, 1554.

[12] Gao, J., Guzzi, M., Huston, J., Lai, H.-L., Li, Z., et al. (2014). The CT10 NNLO Global Analysis of QCD. *Phys.Rev.*, D89, 033009.

[13] Gleisberg, T., Hoeche, S., Krauss, F., Schonherr, M., Schumann, S., et al. (2009). Event generation with SHERPA 1.1. *JHEP*, 0902, 007.

[14] Kauer, N. & Passarino, G. (2012). Inadequacy of zero-width approximation for a light Higgs boson signal.

[15] Mangano, M. L. et al. (2003). ALPGEN, a generator for hard multiparton processes in hadronic collisions. *JHEP*, 0307, 001.

[16] Nason, P. (2004). A new method for combining NLO QCD with shower Monte Carlo algorithms. *JHEP*, 11, 040.

[17] P. M. Nadolsky (2008). Implications of CTEQ global analysis for collider observables. *Phys. Rev.*, D 78, 013004.

[18] S. Agostinelli et al. (2003). Geant4, a simulation toolkit. *Nucl. Instrum. Meth.*, A 506, 250.

[19] Sherstnev, A. & Thorne, R. S. (2009). Parton distributions for the LHC. *Eur. Phys. J*, C 55, 553.

[20] Sjostrand, T., Mrenna, S., & Skands, P. Z. (2006). PYTHIA 6.4 Physics and Manual. *JHEP*, 0605, 026.

[21] Sjostrand, T., Mrenna, S., & Skands, P. Z. (2008). A Brief Introduction to PYTHIA 8.1. *Comput.Phys.Commun.*, 178, 852–867.

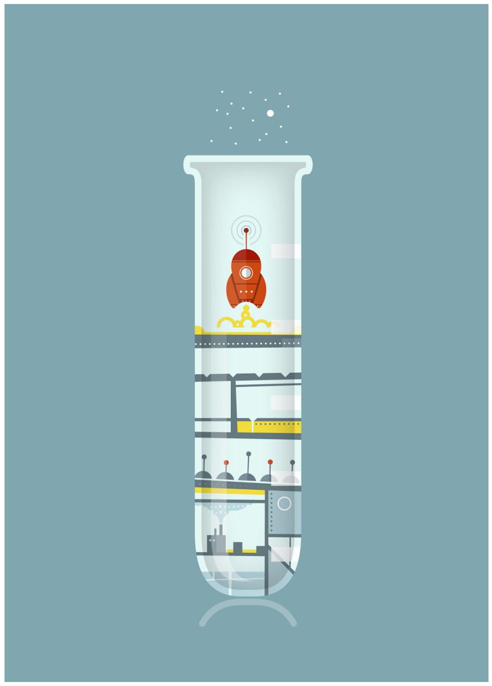

This thesis was typeset using LaTeX, originally developed by Leslie Lamport and based on Donald Knuth's TeX. The body text is set in 11 point Egenolff-Berner Garamond, a revival of Claude Garamont's humanist typeface. The above illustration, *Science Experiment 02*, was created by Ben Schlitter and released under CC BY-NC-ND 3.0. A template that can be used to format a PhD dissertation with this look & feel has been released under the permissive AGPL license, and can be found online at github.com/asm-products/Dissertate or from its lead author, Jordan Suchow, at suchow@post.harvard.edu.